

# Active double emulsions

Babak Vajdi Hokmabad,<sup>1,\*</sup> Kyle A. Baldwin,<sup>1,2,\*</sup> Carsten Krüger,<sup>1</sup> Christian Bahr,<sup>1</sup> and Corinna C. Maass<sup>1,†</sup>

<sup>1</sup>Max Planck Institute for Dynamics and Self-Organization, Am Faßberg 17, 37077 Göttingen

<sup>2</sup>School of Science and Technology, Nottingham Trent University, Nottingham, NG11 8NS, United Kingdom

(Dated: December 15, 2024)

The capability to produce controllable, actively self-propelling microcapsules would present a leap forward in the development of artificial cells, microreactors, and microsensors. Inactive microcapsules have been developed in the form of double emulsions (droplet shells), which have been applied as, *e.g.*, reactive microcontainers [1], synthetic cell membranes [2], food and drug capsules [3, 4], cosmetics [5], optical devices [6–8], and biotic sensors [9]. Despite the wide utility of double emulsions as a platform for synthetic biology and microchemistry, a significant challenge remains in combining activity, stability, and control. Here we demonstrate a new approach to the problem of encapsulation by using active nematic double emulsions, where anisotropic micellar solubilization induces motility, and nematicity provides stability. We further observe a peculiar “shark-fin meandering” swimming that is driven by spontaneously broken symmetries and self-generated chemical fields, which we can control via topology and chemical signalling. These results demonstrate a novel and versatile technique for self-propulsion and cargo delivery, which will open avenues for applications in transport, guidance and targeted release.

Our active double emulsion system is comprised of water-in-oil-in-water droplet shells, where self-propulsion is induced via solubilization in a micellar surfactant solution. This swimming mechanism is based on the established system of active single emulsions [10–13], where self-propulsion is maintained by a self-sustaining surface tension gradient in the oil-water interface [14]. Swimming droplets shed persistent trails of oil-filled micelles, from which they are subsequently repelled [15]. We use the nematogen 5CB as the oil phase, and solutions of the anionic surfactant TTAB (see methods) as the aqueous phases, where the internal core droplet is submicellar ( $c = 0.75$  CMC), and the external swimming medium is supramicellar ( $c > 30$  CMC). We mass-produce highly monodisperse oil droplet shells using consecutive microfluidic cross-junctions in flow-focusing configuration [2].

While controllable self-propulsion is well established in single emulsions [11], we cannot expect the same in double emulsions. Firstly, the second oil-water interface will modify, and possibly impede, the convective flow in the oil phase. Secondly, the internal convection will drive the

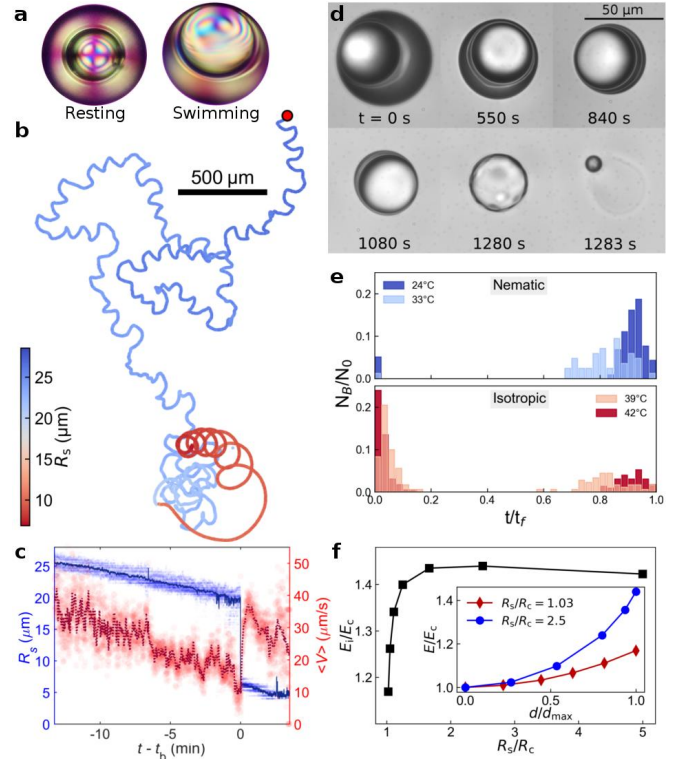


FIG. 1. Life stages and stability of active shells **a**, Polarised images of resting and swimming shell. **b**, Example trajectory coloured by shell radius  $R_s$ , recorded over 40 min. **c**, Average speed  $V$  (dotted, red) and radius  $R_s$  (solid, blue) for 13 shells, time  $t$  relative to bursting time  $t_B$  (scatter plots: experimental error). **d**, Video stills of droplet life stages. **e**, Burst statistics (number of bursts  $N_B$  normalised to initial number of shells  $N_0$ ) for shells below and above the clearing point, plotted against time  $t$  normalised to final time  $t_f$  with no remaining shells ( $t_f(24^\circ\text{C}) \approx 45$  min.,  $t_f(39^\circ\text{C}) \approx 10$  min., initial  $R_s = 30 \mu\text{m}$ ,  $R_c = 18 \mu\text{m}$ ) **f**, Ratio of elastic energies  $E_i/E_c$  ( $E_i$ : core droplet close to outer shell interface,  $E_c$ : core at center) against ratio of radii  $R_s/R_c$ , using  $R_c = 25 \mu\text{m}$  and  $R_s$  shrinking from  $125 \mu\text{m}$  to  $25.6 \mu\text{m}$ . Inset: Elastic energy  $E/E_c$  as a function of core displacement  $d/d_{\text{max}}$ , with  $d_{\text{max}} = R_s - R_c = 100$  nm, for two different ratios  $R_s/R_c$ .

aqueous core towards the shell boundary, promoting coalescence of the aqueous phases (Fig. 1 a). Despite these factors, our shells self-propel stably and reproducibly for long times, dissolving down to thin shells with a minimum stable shell/core radii fraction of  $R_s/R_c \approx 1.01$ , with a thickness on the order of  $\sim 1 \mu\text{m}$ .

The life stages of these self-propelling shells (Fig. 1 b)

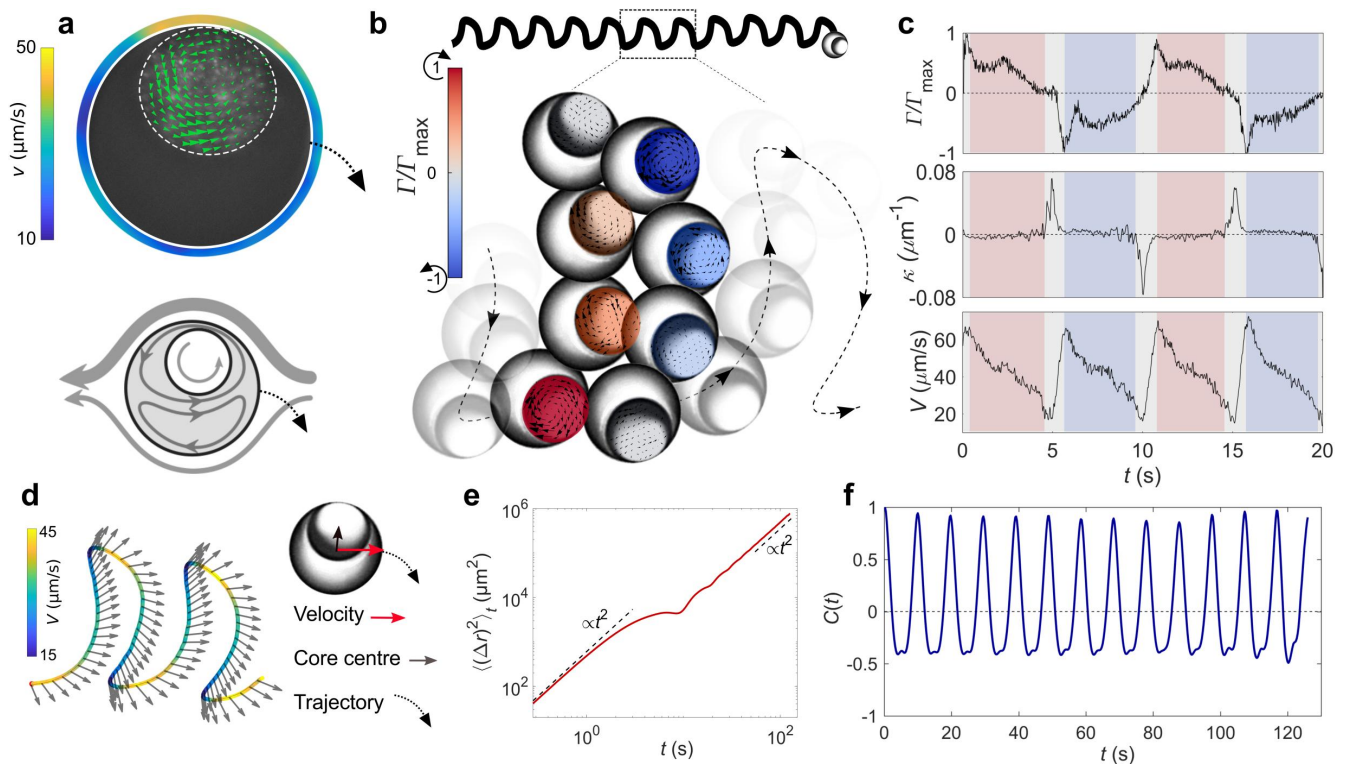


FIG. 2. ‘Shark fin’ meandering example ( $R_s = 36\mu\text{m}$ ): **a**, Top: PIV data for flow at the outer interface and in the core. Bottom: schematic of core and flow arrangement. **b**, Top: ‘shark-fin’ meandering of swimming trajectory over 2 minutes; the shell switches periodically between clockwise and anticlockwise turns. Bottom: zoomed in view of the shell-core alignment with the swimming trajectory, with superimposed core flow fields and colour-coded circulation. **c**, Core circulation  $\Gamma/\Gamma_{\text{max}}$ , local curvature  $\kappa$ , and shell speed  $V$  versus time over four meandering periods. **d**, Trajectory coloured by speed with arrows indicating the core orientation, showing a slowdown before and sudden speedup after the kink. **e**, mean squared displacement and **f**, angular correlation for one trajectory. See also movies S2 and S4.

fall into three regimes: (I) ‘Shark-fin’ meandering. At early times, the core is small compared to the shell diameter (Fig. 1 d, top) and is deflected considerably from the polar axis of the shell, resulting in a meandering instability. (II) *Thin shells*. As the shell thins, eventually there is little room for significant asymmetry in the shell-core arrangement (Fig. 1 d, bottom). During this stage, the motion grows noisy while the speed decreases, until propulsion stops. (III) *Single Emulsion*. On reaching a critical minimum thickness, the shell bursts, reconstituting into a single oil droplet. From a comparison of pre- and post-burst radii, we estimate the average shell thickness at this point to be on the order of  $1\mu\text{m}$  (Fig. 1 c). The droplet then propels with an undisturbed internal convection, leading to a sudden increase in speed, and a curling motion as observed in nematic single emulsions [16] (Fig. 1 b, red).

In contrast to these reproducible stages in nematic shells, we find that under otherwise identical conditions, isotropic shells burst significantly earlier, during the meandering phase. Fig. 1 e shows burst statistics for 5CB shells, where below the clearing point ( $T < 34.5^\circ\text{C}$ , nematic) shells survive for long times, whereas above the

clearing point ( $T > 34.5^\circ\text{C}$ , isotropic), most droplets do not reach the thin shell stage.

We attribute the shell stability to a nematoelastic energy barrier: 5CB molecules arrange to minimise the elastic energy associated with the deviations from a uniform director field imposed by the boundary conditions (here homeotropic anchoring [17]). In a resting shell, this causes a radially symmetric arrangement of the director field [18] with the aqueous core at the centre. In a moving shell the internal flow drives the core off-centre: the director field is therefore distorted both by the displacement of the core and the flow field, such that the elastic energy is increased.

To estimate the competing forces we numerically calculated the elastic energy  $E$  stored in a resting shell with a core displaced by a distance  $d$ . We find that  $E$  increases by a factor of  $E_i/E_c \approx 1.4$  when the core droplet is located at the outer interface ( $E = E_i, d = d_{\text{max}}$ ), as compared to the centered configuration ( $E = E_c$ ). Remarkably, we find only a minor dependence on the thickness of the nematic shell.  $E_i/E_c$  drops significantly towards unity only for  $R_s/R_c < 1.1$  (Fig. 1 f), *i.e.*, the elastic energy barrier vanishes only in the limit of zero

shell thickness.

We calculate the elastic force  $F_e = \partial E / \partial d$  acting on a core displaced to the boundary of a 5CB shell [19, 20] to be of the order of  $\approx 100$  pN. This is equivalent to the Stokes drag [14],

$$F_S = 2\pi R_c v \frac{2\eta_{5CB} + 3\eta_{aq}}{1 + \eta_{aq}/\eta_{5CB}}, \quad (1)$$

acting on an aqueous core moving through bulk 5CB at  $v \approx 6 \mu\text{m/s}$ , which is comparable to the velocity of the convective flow in our shells. We propose that the nematic-to-elastic repulsion provides a significant, although not insurmountable, barrier against coalescence (Fig. 1 e).

We have analysed the meandering dynamics by simultaneously tracking the core circulation  $\Gamma(t)$ , local trajectory curvature  $\kappa(t)$ , and propulsion speed  $V(t)$  (Fig. 2 a–d). In quasi-2D confinement, the core is trapped off-axis inside the convective torus, where it co-rotates with the convective flow, as shown by the core flow and colour coded  $\Gamma$  values in Fig. 2 a, b. In this arrangement, there is less viscous resistance to the driving interfacial flows in the part of the shell containing the core, resulting in asymmetric flow with respect to the direction of motion (shown by the colour bar in Fig. 2 a), and a curved trajectory.

This eventually curves the shell back towards its own trail, where chemotactic repulsion causes  $V$  and  $\Gamma$  to slowly decay and then abruptly reverse - the tip of the ‘shark fin’ motion (Fig. 2 b, d). This abrupt reorientation corresponds to a spike in the local curvature and is followed by a sharp acceleration (Fig. 2 c), caused by repulsion from the local gradient of filled micelles. Due to the flow reversal, in the reference frame of the droplet the core has now switched sides and the shell curves in the opposite direction, once again towards its own trail.

We distinguish three time scales: a short timescale ( $\approx 1$  s) for autochemotactically driven abrupt reorientation (Fig. 2 c), an intermediate timescale ( $\approx 5$  s) for the curved motion between two shark-fin tips, and a long timescale ( $> 100$  s) corresponding to the persistent motion imposed by the chemical field in the trail of the shell, as shown by the mean squared displacement  $\langle(\Delta r)^2\rangle_t$  and the angular autocorrelation  $C(t)$  (Fig. 2 e, f).

To investigate the role of the core in breaking the flow symmetry, we have compared the 3D motion of droplets with zero, one and two cores in a density matched medium (Fig. 3 a). With no core, we reproduce previous findings [16], where the displacement of the radial ‘hedgehog’ defect induces a torque on the droplet, resulting in helical trajectories. With one core, we observe similar behaviour. Escaping to the third dimension, the droplet is not arrested by its own trail and does not reverse its direction. Instead, the core precesses around the axis of motion. These shells propel in more tightly wound helices than single emulsions, which can be understood in terms of the torque applied by the respective

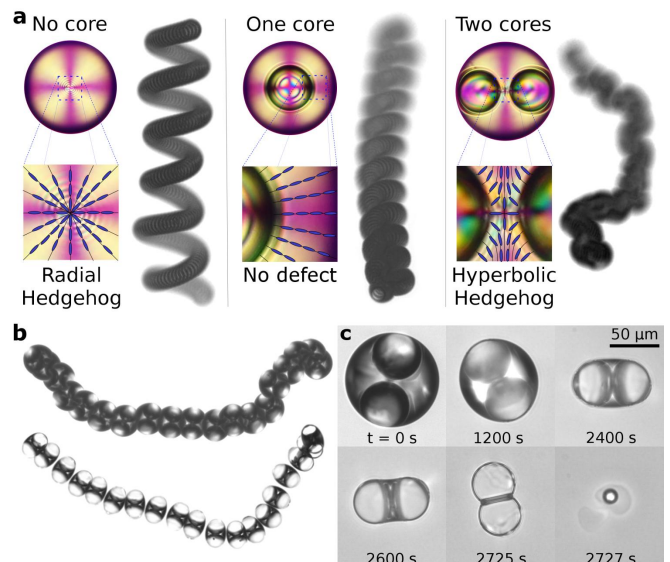


FIG. 3. Droplet topology. **a**, Comparison of 3D swimming trajectories (multiple exposure track of single swimmer) over a 60 s period for a single emulsion droplet (left,  $R_s = 37 \mu\text{m}$ ), a single core shell (middle,  $R_s = 50 \mu\text{m}$ ) and a double core shell (right,  $R_s = 62 \mu\text{m}$ ). Insets are images of respective droplet types as viewed at rest under cross-polarized microscopy, and zoomed in views that schematically show the nematic structure. **b**, Life stages of an active double-core shell. **c**, Swimming trajectories of the double core shown in **b** for thick (top) and thin (bottom) shells, over 45 s. Data in (b,c) taken from movie S5.

viscous anisotropy: in the shells considered here, it is the viscosity ratio of oil and water,  $\eta_2(5CB)/\eta(\text{H}_2\text{O}) \approx 50$ ; in contrast, for the single emulsions studied in [16], it refers to the intrinsic viscous anisotropy of a nematic liquid crystal  $\eta_2(5CB)/\eta_{\text{iso}}(5CB) \approx 3$  [20]. With two cores, we do not expect this broken symmetry argument to hold. While a single-core nematic shell is defect free and spherically symmetric at rest, double core shells have a fixed axis set by the two cores, with a topological charge of  $+1$  resolved by a hyperbolic hedgehog defect, or a defect loop [21–23]. This defect provides a barrier against core coalescence [24]. The most likely flow field configuration inside a moving double-core shell is with both cores trapped on opposite sides of the convection torus and no symmetry breaking mechanism or curling. Instead, the shell moves perpendicularly to the core alignment, with some rotational fluctuations (demonstrated in quasi-2D, Fig. 3 b). As in the single-core case, the shell thickness shrinks to  $\approx 1 \mu\text{m}$  until the shell bursts (Fig. 3 c).

To provide avenues towards targeted delivery, we demonstrate two methods for guiding self-propelling shells. First, topographical guidance: Fig. 4 a shows a shell swimming along a wall [25], turning both convex and concave corners. PIV data (Fig. 4 c) shows that for such a shell the flow is fastest at the interface furthest from the wall, which coincides with the position of the

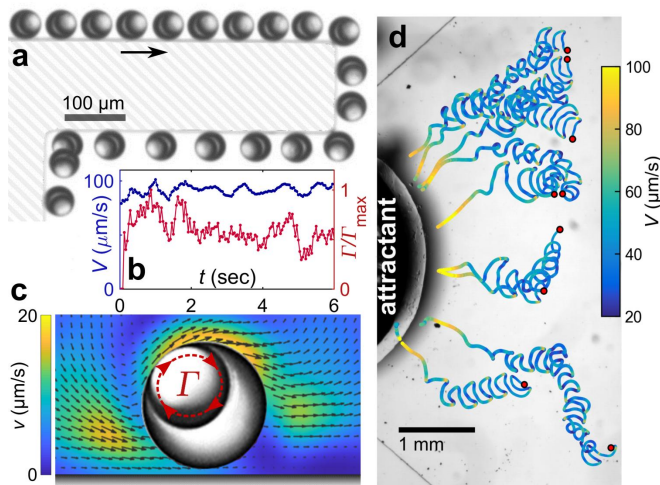


FIG. 4. Shell guidance. **a**, Topographical guidance by walls: multiple exposure micrograph over 65 s. **b**, Plot of swimming speed  $V$  and core circulation  $\Gamma$  when moving parallel to a wall (cf. Fig. 2c). **c**, Flow field  $\vec{v}$  around the shell near a wall, mapped by PIV. **d**, Chemotaxis: diffusing surfactant guides shells to the left (trajectories coloured by shell speed  $V$ ).

core. This provides a torque on the droplet, directed towards the wall, stabilizing wall alignment. In contrast to the meandering case,  $\Gamma$  and  $V$  are constant (Fig. 4b), as the wall prevents the shell from curling towards its own trail.

Second, chemotactic guidance: as with single emulsions [15], shells follow external surfactant concentration gradients. In Fig. 4d, crystalline surfactant (‘attractant’) is allowed to dissolve into a Hele-Shaw cell. The resulting gradient extends  $\approx 1$  mm into the cell, attracting the shells, doubling their speed and rectifying the meandering instability.

In conclusion, we show that active double emulsions can be utilised as a targeted cargo delivery system, which can be guided by chemical signals and topography. While active isotropic shells are susceptible to premature coalescence, we find that nematoelasticity provides stability. This can be utilised in designing microreactors and artificial cells - for example, light-switchable nematogens are an ideal candidate for externally activated release capsules. We further anticipate that the understanding of the rich swimming dynamics, including the novel shark-fin meandering state, will impact the design of artificial or robotic microswimmers, where the behaviour can be tweaked by tuning the routes for spontaneous symmetry breaking in otherwise symmetrically simple swimmers.

*Author contributions and acknowledgments:* KAB and BVH designed and conducted experiments, analysed data and wrote the paper; CK conducted experiments; CB performed numerical calculations and wrote the paper; CCM designed experiments, analysed data

and wrote the paper. We acknowledge J. Petit for experimental setup expertise, S. Herminghaus for discussions, and the Max Planck Society and the German Research Foundation (DFG) Priority Programme SPP1726 ‘‘Microswimmers’’ for project and personnel funding.

\* KAB and BVH contributed equally

† electronic address: corinna.maass@ds.mpg.de

- [1] E. Lorenceau, A. S. Utada, D. R. Link, G. Cristobal, M. Joanicot, and D. A. Weitz, ‘‘Generation of Polymerosomes from Double-Emulsions,’’ *Langmuir*, vol. 21, no. 20, pp. 9183–9186, 2005.
- [2] J. Petit, I. Polenz, J.-C. Baret, S. Herminghaus, and O. Bäumchen, ‘‘Vesicles-on-a-chip: A universal microfluidic platform for the assembly of liposomes and polymerosomes,’’ *Eur. Phys. J. E.*, vol. 39, no. 6, p. 59, 2016.
- [3] M. A. Augustin and Y. Hemar, ‘‘Nano- and microstructured assemblies for encapsulation of food ingredients,’’ *Chem. Soc. Rev.*, vol. 38, no. 4, pp. 902–912, 2009.
- [4] S.-H. Kim, J. W. Kim, J.-C. Cho, and D. A. Weitz, ‘‘Double-emulsion drops with ultra-thin shells for capsule templates,’’ *Lab Chip*, vol. 11, no. 18, pp. 3162–3166, 2011.
- [5] V. B. Patravale and S. D. Mandawgade, ‘‘Novel cosmetic delivery systems: An application update,’’ *Int. J. Cosmetic Sci.*, vol. 30, no. 1, pp. 19–33, 2008.
- [6] L. Chen, Y. Li, J. Fan, H. K. Bisoyi, D. A. Weitz, and Q. Li, ‘‘Photoresponsive Monodisperse Cholesteric Liquid Crystalline Microshells for Tunable Omnidirectional Lasing Enabled by a Visible Light-Driven Chiral Molecular Switch,’’ *Adv. Opt. Mater.*, vol. 2, no. 9, pp. 845–848, 2014.
- [7] S. Nagelberg, L. D. Zarzar, N. Nicolas, K. Subramanian, J. A. Kalow, V. Sresht, D. Blankschtein, G. Barbastathis, M. Kreysing, T. M. Swager, and M. Kolle, ‘‘Reconfigurable and responsive droplet-based compound microlenses,’’ *Nat. Commun.*, vol. 8, p. 14673, 2017.
- [8] L. D. Zarzar, V. Sresht, E. M. Sletten, J. A. Kalow, D. Blankschtein, and T. M. Swager, ‘‘Dynamically reconfigurable complex emulsions via tunable interfacial tensions,’’ *Nature*, vol. 518, no. 7540, pp. 520–524, 2015.
- [9] Q. Zhang, S. Savagatrup, P. Kaplonek, P. H. Seeberger, and T. M. Swager, ‘‘Janus Emulsions for the Detection of Bacteria,’’ *ACS Cent. Sci.*, vol. 3, no. 4, pp. 309–313, 2017.
- [10] S. Thutupalli, R. Seemann, and S. Herminghaus, ‘‘Swarming behavior of simple model squirmers,’’ *New J. Phys.*, vol. 13, no. 7, p. 73021, 2011.
- [11] C. C. Maass, C. Krüger, S. Herminghaus, and C. Bahr, ‘‘Swimming Droplets,’’ *Annu. Rev. Condens. Matter Phys.*, vol. 7, no. 1, pp. 171–193, 2016.
- [12] Z. Izri, M. N. van der Linden, S. Michelin, and O. Dautchot, ‘‘Self-Propulsion of Pure Water Droplets by Spontaneous Marangoni-Stress-Driven Motion,’’ *Phys. Rev. Lett.*, vol. 113, no. 24, p. 248302, 2014.
- [13] M. Li, M. Brinkmann, I. Pagonabarraga, R. Seemann, and J.-B. Fleury, ‘‘Spatiotemporal control of cargo delivery performed by programmable self-propelled Janus droplets,’’ *Commun. Phys.*, vol. 1, no. 1, p. 23, 2018.

- [14] S. Herminghaus, C. C. Maass, C. Krüger, S. Thutupalli, L. Goehring, and C. Bahr, “Interfacial mechanisms in active emulsions,” *Soft Matter*, vol. 10, no. 36, pp. 7008–7022, 2014.
- [15] C. Jin, C. Krüger, and C. C. Maass, “Chemotaxis and autochemotaxis of self-propelling droplet swimmers,” *P. Natl. Acad. Sci. USA*, vol. 114, no. 20, pp. 5089–5094, 2017.
- [16] C. Krüger, G. Klös, C. Bahr, and C. C. Maass, “Curling Liquid Crystal Microswimmers: A Cascade of Spontaneous Symmetry Breaking,” *Phys. Rev. Lett.*, vol. 117, no. 4, p. 048003, 2016.
- [17] J. M. Brake, A. D. Mezera, and N. L. Abbott, “Effect of surfactant structure on the orientation of liquid crystals at aqueous-liquid crystal interfaces,” *Langmuir*, vol. 19, no. 16, pp. 6436–6442, 2003.
- [18] T. Lopez-Leon and A. Fernandez-Nieves, “Drops and shells of liquid crystal,” *Colloid Polym. Sci.*, vol. 289, pp. 345–359, 2011.
- [19] P. P. Karat and N. V. Madhusudana, “Elasticity and Orientational Order in Some 4'-n-Alkyl-4-Cyanobiphenyls: Part II,” *Mol. Cryst. Liq. Cryst.*, vol. 40, no. 1, pp. 239–245, 1977.
- [20] A. G. Chmielewski, “Viscosity Coefficients of Some Nematic Liquid Crystals,” *Mol. Cryst. Liq. Cryst.*, vol. 132, no. 3-4, pp. 339–352, 1986.
- [21] N. D. Mermin, “The topological theory of defects in ordered media,” *Rev. Mod. Phys.*, vol. 51, no. 3, pp. 591–648, 1979.
- [22] T. C. Lubensky, D. Petey, N. Currier, and H. Stark, “Topological defects and interactions in nematic emulsions,” *Phys. Rev. E*, vol. 57, no. 1, pp. 610–625, 1998.
- [23] P. Poulin and D. A. Weitz, “Inverted and multiple nematic emulsions,” *Phys. Rev. E*, vol. 57, no. 1, pp. 626–637, 1998.
- [24] P. Poulin, H. Stark, T. C. Lubensky, and D. A. Weitz, “Novel colloidal interactions in anisotropic fluids,” *Science*, vol. 275, no. 5307, p. 1770, 1997.
- [25] C. Jin, B. Vajdi Hokmabad, K. A. Baldwin, and C. C. Maass, “Chemotactic droplet swimmers in complex geometries,” *J. Phys.: Condens. Mat.*, vol. 30, no. 5, p. 054003, 2018.
- [26] D. Qin, Y. Xia, and G. M. Whitesides, “Soft lithography for micro- and nanoscale patterning,” *Nat. Protoc.*, vol. 5, no. 3, pp. 491–502, 2010.
- [27] A. Schmit, L. Salkin, L. Courbin, and P. Panizza, “Commensurability-driven structural defects in double emulsions produced with two-step microfluidic techniques,” *Soft Matter*, vol. 10, no. 26, pp. 4743–8, 2014.
- [28] J. C. Crocker and D. G. Grier, “Methods of digital video microscopy for colloidal studies,” *J Colloid Interface Sci*, vol. 179, pp. 298–310, 1996.
- [29] W. Thielicke and E. Stamhuis, “PIVlab – Towards User-friendly, Affordable and Accurate Digital Particle Image Velocimetry in MATLAB,” *JORS*, vol. 2, no. 1, p. e30, 2014.
- [30] H. Wioland, F. G. Woodhouse, J. Dunkel, and R. E. Goldstein, “Ferromagnetic and antiferromagnetic order in bacterial vortex lattices,” *Nat Phys*, vol. 12, pp. 341–345, 2016.
- [31] H. Mori, J. Eugene C. Gartland, J. R. Kelly, and P. J. Bos, “Multidimensional Director Modeling Using the Q Tensor Representation in a Liquid Crystal Cell and Its Application to the  $\pi$  Cell with Patterned Electrodes,” *Jpn. J. Appl. Phys.*, vol. 38, no. 1R, p. 135, 1999.
- [32] M. Ravnik and S. Žumer, “Landau–de Gennes modelling of nematic liquid crystal colloids,” *Liq. Cryst.*, vol. 36, no. 10-11, pp. 1201–1214, 2009.
- [33] P.-G. De Gennes, “Short Range Order Effects in the Isotropic Phase of Nematics and Cholesterics,” *Mol. Cryst. Liq. Cryst.*, vol. 12, no. 3, pp. 193–214, 1971.

## METHODS

### Double emulsion fabrication

Our emulsions comprise the nematic liquid crystal 4-pentyl-4'-cyano-biphenyl (5CB) and an aqueous solution of the surfactant tetradecyltrimethylammonium bromide (TTAB). Where required, we match the densities between the oil ( $\rho_{5CB} = 1.022 \text{ g ml}^{-1}$  at  $24^\circ\text{C}$ ) and surfactant solution phases by  $\text{D}_2\text{O}$  ( $\rho_{\text{D}_2\text{O}} = 1.107 \text{ g ml}^{-1}$ ) admixture, with adjustments for TTAB content. In separate experiments, we created isotropic double emulsions, using: the branched 5CB isomer CB15 ((S)-4-Cyano-4'-(2-methylbutyl)biphenyl, Syntho Chemicals); and 10:1 volumetric ratio of 5CB and BPD (Bromopentadecane, Sigma-Aldrich). These shells were highly unstable when active, and were not examined further.

We generate and observe double emulsion droplets in microfluidic PDMS chips on glass slides; fabricated in-house using standard soft lithography methods[26]. We follow the recipe of Petit *et al.* [2] for creating monodisperse water-in-oil-in-water emulsions, where the chips consist of two sequential cross-shaped flow junctions, for water-in-oil followed by oil-in-water droplet pinch-off (Fig. S1). The number of cores, as well as the core and shell diameters, are set by the flow rates [27]. Shell and core radii were produced in the range of  $R_s = 20\text{-}130 \mu\text{m}$  and  $R_c = 10\text{-}50 \mu\text{m}$  respectively. Typical flow rates were in the ranges 10-30, 60-150, and 200-500  $\mu\text{l hr}^{-1}$  for the core aqueous phase, oil phase, and external aqueous phase respectively.

To ensure the oil phase did not wet the initially hydrophobic PDMS walls, the outer flow channels were hydrophilized prior to droplet production. This was achieved by drawing a sequence of liquids through the outermost channel via a vacuum pump induced pressure gradient. The sequence was as follows: a 1:1 volumetric ratio of hydrochloric acid (HCl at 37 wt.%, Sigma-Aldrich) and hydrogen peroxide ( $\text{H}_2\text{O}_2$  at 30 wt.%, Sigma-Aldrich) for 2 minutes; Milli-Q water for 30 seconds; 5 wt.% aqueous solution of poly(diallyldimethylammonium chloride) (PDADMAC, average molecular weight  $M_w \approx 100,000\text{-}200,000 \text{ g mol}^{-1}$ , Sigma-Aldrich), for 2 minutes; 2 wt.% aqueous solution of poly(sodium 4-styrenesulphonate) (PSS,  $M_w \approx 1,000,000 \text{ g mol}^{-1}$ , Sigma-Aldrich) for 2 minutes.

During production and in storage, both the internal and external aqueous phases contain a submicellar concentration of TTAB (0.1 wt.%): sufficient to stabilise the interface, but insufficient to induce solubilisation (CMC = 0.13 wt.%). 5CB double emulsion droplets at room temperature ( $T = 24^\circ\text{C}$ ) are stable against coalescence for several months.

### Observation and analysis

For polarized microscopy we used a Nikon Eclipse LV100 Polarizing microscope equipped with a digital camera (EOS 600d, Canon). Crossed polarizers with an added  $\lambda$  retardation plate were used to visualize the nematic director field inside the liquid crystal phase. We used two inverted microscopes (Olympus IX-73 and IX-81) with either a Grasshopper (GS3-U3-41C6M-C) grayscale camera ( $2048 \times 2048$  pixels) or a Canon (EOS 600d) digital camera ( $1920 \times 1080$  pixels) for regular visible light microscopy recording images at 4-24 fps and  $4\text{-}40\times$  magnification for tracking the swimmers. The fluorescent imaging was done on an IX-73 inverted microscope at 24 fps and  $20\times$  magnification for PIV measurements around the shells and at 48 fps and  $40\times$  magnification for PIV inside the core. We extracted shell positions from video microscopy data using standard Python libraries for numpy, PIL and opencv (Scripts available on request). Essential steps are background correction, binarisation, blob detection by contour analysis and minimum enclosing circle fits. We calculated trajectories and speeds using a simple next neighbour algorithm [28]. We identified bursting times by frame-by-frame inspection. We estimated core position and orientation angles from high resolution video data by semi-automatically determining circular shell and core outlines and comparing the line of centres to the trajectory normal. The mean squared displacement of the shell trajectory was calculated as

$$\langle(\Delta r)^2\rangle_t = \langle[\mathbf{r}(t_0 + t) - \mathbf{r}(t_0)]^2\rangle_{t_0}, \quad (2)$$

where  $\mathbf{r}$  is the position vector of the shell. The angular or velocity autocorrelation function was calculated as

$$C(t) = \left\langle \frac{V(t_0 + t) \cdot V(t_0)}{|V(t_0 + t)| |V(t_0)|} \right\rangle_{t_0}, \quad (3)$$

and the (signed) local curvature of the trajectory was defined as

$$\kappa = \frac{x'y'' - y'x''}{(x'^2 + y'^2)^{3/2}}, \quad (4)$$

where the prime denotes derivation with respect to time.

For the PIV analyses in Fig. 2 a and Fig. 4 b. the shell was pinned in a shallow cell and the aqueous phase was

seeded with  $0.5\ \mu\text{m}$  fluorescent tracer colloids (Thermo Fisher Scientific). For PIV inside the core, the core was seeded with the same tracers, the core position was tracked manually and the time-resolved PIV images were collected. All PIV analyses and flow calculations were performed via the MATLAB based PIVlab interface [29]. Additional custom MATLAB scripts were written to calculate the circulation of the flow inside the internal aqueous droplet [30]:

$$\Gamma_i(t) = \hat{\mathbf{z}} \cdot \left[ \sum_{(x,y)_i} \mathbf{r}_i(x,y) \times \mathbf{u}(x,y,t) \right], \quad (5)$$

where  $\mathbf{r}_i$  is the vector from the core center to  $(x,y)$  inside the projected area of the core on the x-y plane.

### Numerical calculations

The elastic energy estimates plotted in Fig. 1 f were calculated via the following principles: We applied a common numeric minimisation technique [31, 32] based on the  $\mathbf{Q}$  tensor representation of the nematic director field [33]. The one-constant approximation of the nematic elasticity was used, setting the value of the elastic constant  $K$  to  $6.4\ \text{pN}$  ( $= K_{\text{display}}$  of 5CB). We assumed strict homeotropic anchoring of the director at all interfaces, *i.e.*, the orientation of the nematic director at the interface is set perpendicular to the interface and held constant (so-called strong anchoring conditions). The droplet volume is mapped onto a cubic grid with  $256^3$  nodes. Details of the numerical procedures are given in [31].

## SUPPORTING INFORMATION

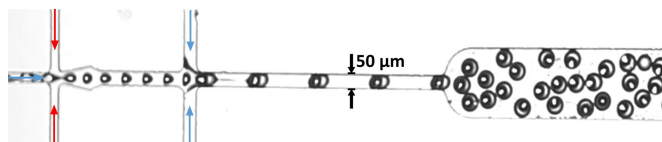


FIG. S1. Screenshot of a microfluidic chip producing double emulsion droplets ( $R_s \approx 30 \mu\text{m}$ ). Blue and red arrows indicate flow of aqueous and oil phases respectively. The channel height is  $50 \mu\text{m}$ .

The following movies are available for viewing under <http://asm.ds.mpg.de/index.php/media/>. Direct download links are provided in the preview captions.



FIG. S2. Movie S2 showing one shell ( $R_s \approx 30 \mu\text{m}$ , 131 s, speed x6 at 24 fps) shark-fin meandering, with high persistence and periodicity, as well as a “curling” single emulsion droplet, in a uniform bulk environment.  
<http://asm.ds.mpg.de/wp-content/uploads/2019/01/movie2oneshark.mp4>

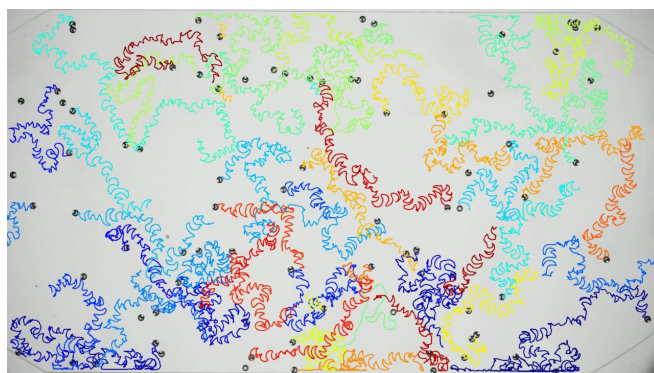


FIG. S3. Movie S3 showing selected trajectories for an ensemble of shark-fin meandering shells (500 s, speed x25 at 10 fps, field of view  $5.4 \times 3 \text{ mm}$ ).  
<http://asm.ds.mpg.de/wp-content/uploads/2018/10/movie1sharkfin.mp4>

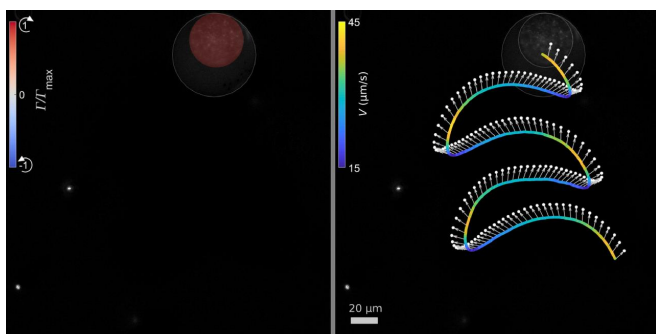


FIG. S4. Movie S4 (255 s, speed x1 at 24 fps) tracking circulation, speed and core orientation for a meandering shell, data corresponding to Fig. 2 b, d.

<http://asm.ds.mpg.de/wp-content/uploads/2019/01/movie4circulation-speed.mp4>

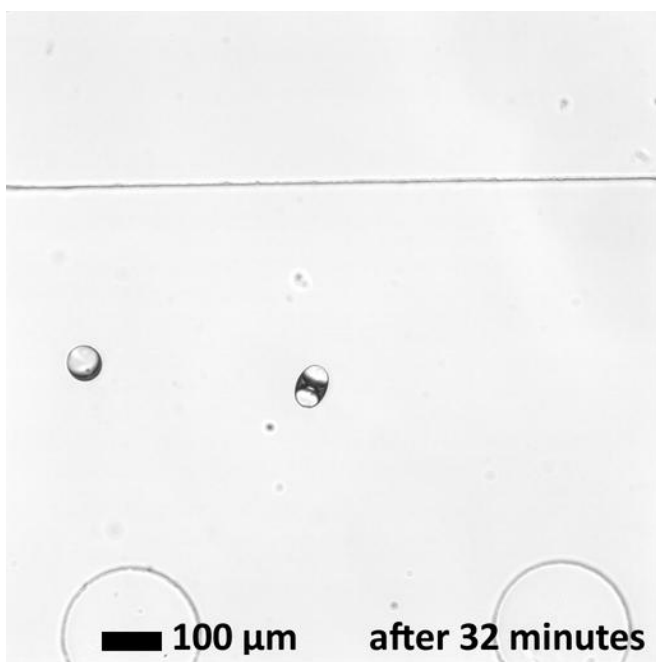


FIG. S5. Movie S5 (speed x12 at 24 fps) showing the dynamics and life stages of a double core shell (see Fig. 3 for shell sizes). <http://asm.ds.mpg.de/wp-content/uploads/2019/01/movie2doublecore.mp4>